Chemical Geology 660 (2024) 122150

Contents lists available at ScienceDirect

Chemical Geology

journal homepage: www.elsevier.com/locate/chemgeo

Low Mo mobility during the laterization of ultramafic bedrock: Evidence from the East Sulawesi Ophiolite, Indonesia

Adrianus Damanik [a,b,*], Martin Wille [a], Qasid Ahmad [a,d], Sukalpa Chatterjee [a], Sean A. Crowe [e,f], Kohen W. Bauer [g], Martin Grosjean [b,h], Sri Yudawati Cahyarini [c], Satria Bijaksana [i], James M. Russell [j], Hendrik Vogel [a,b]

[a] Institute of Geological Sciences, University of Bern, Baltzerstrasse 1+3, Bern 3012, Switzerland
[b] Oeschger Centre for Climate Change Research, University of Bern, Hochschulstrasse 4, Bern 3012, Switzerland
[c] Paleoclimate & Paleoenvironment Research Group-Research Center of Climate and Atmosphere, National Research and Innovation Agency (BRIN), Jalan Sangkuriang, Bandung 40135, Indonesia
[d] Centre de Recherches Pétrographiques et Géochimiques (CRPG), CNRS, Nancy UMR, 7358, France
[e] Department of Earth, Ocean, and Atmospheric Sciences, University of British Columbia, Health Sciences Mall, Vancouver 2350, Canada
[f] Department of Microbiology and Immunology, University of British Columbia, Health Sciences Mall, Vancouver 2350, Canada
[g] Ocean Networks Canada, University of Victoria, Ocean-Climate Building #100, Arbutus Road Victoria, BC 2474, Canada
[h] Institute of Geography, University of Bern, Hallerstrasse 12, Bern 3012, Switzerland
[i] Faculty of Mining and Petroleum Engineering, Institut Teknologi Bandung, Jalan Ganesha 10, Bandung 40132, Indonesia
[j] Department of Earth, Environmental, and Planetary Sciences, Brown University, 324 Brook St., Providence, RI 02912, USA

ARTICLE INFO

Editor: Dr. Karen Johannesson

Keywords:
Mo cycling
Mo isotope fractionation
Ultramafic bedrock
Laterization
Fe (oxyhydr)oxides

ABSTRACT

Mo (isotope) cycling during the chemical weathering of ultramafic bedrock remains poorly quantified, mainly as a result of the analytical challenges caused by low Mo concentration and complex matrix effects in these rock types. Here, we utilize an improved chemical separation protocol that enables the extraction of Mo while reducing Ru and Fe matrix effects. We apply this method to lateritic weathering profiles developed over ultramafic bedrock in a high-intensity tropical weathering regime. The Mo concentrations in the laterite samples are higher (0.022 to 0.58 $\mu g \cdot g^{-1}$) than those of the peridotite bedrock (0.006 to 0.021 $\mu g \cdot g^{-1}$). The concentration-weighted average δ^{98}Mo of the laterite profiles is −0.05‰ ($n = 17$), which is slightly higher but very close to the average δ^{98}Mo of the peridotite bedrock (0.17 ± 0.21‰; 2SD; $n = 5$). Weakly-laterized samples show somewhat low δ^{98}Mo with a minimum of −1.03‰ and $\Delta^{98}Mo_{laterite\text{-}bedrock}$ up to −0.86‰, possibly as a result of preferential adsorption of liberated light Mo onto Fe (oxyhydr)oxides. In contrast, strongly-laterized samples show an overall Mo concentration gain and a slight isotopic shift towards higher bulk δ^{98}Mo, with a maximum δ^{98}Mo of +0.12‰ and $\Delta^{98}Mo_{laterite\text{-}bedrock}$ up to +0.42‰. This likely reflects the re-scavenging of Mo released from weakly-laterized horizons to the ubiquitous Fe (oxyhydr)oxides, with potential superimposition of additional heavy Mo from atmospheric and/or groundwater input. Overall, this suggests a small contribution of dissolved Mo derived from ultramafic bedrock weathering in tropical settings to the aquatic environment.

1. Introduction

Molybdenum concentrations ([Mo]) and its stable isotope ratios (in this study: δ^{98}Mo relative to NIST SRM 3134 = 0‰) in marine sediments are known for their potential to record changes in redox conditions (Kendall et al., 2017 and references therein). Both Mo concentration and isotopes are affected by redox-dependent aqueous Mo speciation, aqueous mobility, and interaction/adsorption with solid phases that can be accompanied by significant stable isotope fractionation (Kendall et al., 2017). Under fully oxygenated ocean conditions, dissolved Mo as MoO_4^{2-} is a conservative element (~105 nmol L^{-1}) with a residence time of ~440 to 780 kyrs (Collier, 1985; Colodner et al., 1995; Emerson and Huested, 1991; Miller et al., 2011). The homogenous Mo isotopic composition of the present-day ocean (δ^{98}Mo of = ~+2.09 ± 0.10‰; Barling et al., 2001; Nakagawa et al., 2012; Siebert et al., 2003) is a consequence of a steady state between dissolved Mo input dominated by

* Corresponding author at: Institute of Geological Sciences, University of Bern, Baltzerstrasse 1+3, Bern 3012, Switzerland.
E-mail address: adrianus.damanik@unibe.ch (A. Damanik).

https://doi.org/10.1016/j.chemgeo.2024.122150
Received 21 February 2024; Received in revised form 3 May 2024; Accepted 8 May 2024
Available online 9 May 2024

continental discharge and marine Mo burial in sediments. Therefore, in order to use δ^{98}Mo in marine sediments to reconstruct the global anoxic-oxic Mo sedimentation ratio, a detailed understanding of the global continental river discharge Mo isotope signature is crucial (Kendall et al., 2017).

Compared to the rather homogenous Mo isotope composition of the upper continental crust (+0.05 to +0.15‰; Bezard and Guo, 2023; Greber et al., 2014; Voegelin et al., 2014; Willbold and Elliott, 2017; Yang et al., 2017), rivers show a more variable and overall high dissolved δ^{98}Mo ranging from −0.35 to +2.88‰ (Archer and Vance, 2008; Horan et al., 2020; Neubert et al., 2011; O'Sullivan et al., 2021; Pearce et al., 2010; Voegelin et al., 2012; Wang et al., 2015). Different conditions and processes have been proposed as causes of this δ^{98}Mo variability, including inputs from anthropogenic, hydrothermal, and glacial sources (Neubert et al., 2011; O'Sullivan et al., 2021; Voegelin et al., 2012). Nevertheless, isotopic fractionation during partial adsorption-desorption processes of dissolved Mo onto mineral phases has been identified as the common often predominant process affecting the isotopic variability of dissolved Mo in rivers. Consequently, the overall higher δ^{98}Mo of rivers compared to the upper continental crust implies that, on a global average, soils and river sediments are a reservoir of isotopically light Mo (Archer and Vance, 2008; Horan et al., 2020; Pearce et al., 2010).

Across different weathering regimes with different catchment lithology, morphology, and climate parameters, several processes have been suggested to affect Mo isotope fractionation during soil formation (Greaney et al., 2021; King et al., 2016; Liu et al., 2020; Pearce et al., 2010; Siebert et al., 2015; Wang et al., 2015, 2018, 2020). The Mo isotope variability within weathering profiles depends on different weathering susceptibilities of primary mineral phases hosting Mo. The elevated weatherability of magmatic sulfides with high δ^{98}Mo has been suggested to contribute to a heavy dissolved Mo load relative to the protolith (Voegelin et al., 2012). The high weathering resistance of Fe-Ti oxides, which host isotopically light Mo, accounts for low δ^{98}Mo in weathering profiles relative to the protolith (Wang et al., 2020). However, the formation of secondary mineral phases such as Fe-Mn (oxyhydr)oxides and/or the presence of organic matter (OM) play a major role in controlling [Mo] and δ^{98}Mo variability during soil formation (Goldberg et al., 1996; King et al., 2016; Liu et al., 2020; Siebert et al., 2015; Wang et al., 2018). Particularly, the adsorption of isotopically light Mo from solution onto Fe-Mn (oxyhydr)oxides that form during weathering leads to an isotopically heavy dissolved Mo reservoir (Goldberg et al., 1996; Liu et al., 2020; Wang et al., 2018). Moreover, the complexation of dissolved Mo with OM has been invoked as an important process for the retention of Mo resulting in higher soil [Mo] and δ^{98}Mo relative to the bedrock (King et al., 2016; Liu et al., 2020; Siebert et al., 2015). In addition, external Mo sources can contribute to the overall Mo concentration and isotopic composition of the weathering profile. Groundwater and atmospheric inputs can contribute to the Mo input, and both are typically enriched in the heavy Mo isotopes (King et al., 2016; Nägler et al., 2020; Neely et al., 2018). These external inputs have been identified as potentially large contributors to [Mo] and δ^{98}Mo in soils in certain settings (King et al., 2016; Siebert et al., 2015; Wang et al., 2020).

To first order, the initial [Mo] and δ^{98}Mo of the bedrock define the extent to which all of the processes mentioned above control the aqueous Mo mobility and therefore isotope variability during soil formation. Ultramafic rocks make up only 1.3% of today's continental crust (Beinlich et al., 2018) and contain low Mo concentrations compared to more evolved rocks. As a result, the weathering of ultramafic bedrock is unlikely to be a major source of dissolved Mo globally today. However, this may have been different in the past with evidence of a higher mafic contribution of about 10 wt% to the Archean continental crust (Ptáček et al., 2020). Furthermore, soil that is developed from bedrock with low Mo concentrations is potentially more prone to shifts in the bulk Mo isotopic composition due to the addition of Mo from external sources with a different Mo isotope composition and the effects of secondary mineral formation on Mo mobility and isotope fractionation potentially become more apparent. Studies investigating controls on the behavior of Mo in weathering profiles overlying ultramafic bedrock remain scarce. This may stem from the analytical challenges caused by extremely low Mo contents leading to high Fe/Mo and Ru/Mo ratios in these systems that complicate chemical purification of Mo from the rock matrix essential for precise measurement of Mo isotope differences. Here, we explore the behavior of Mo and its isotopes in lateritic weathering profiles overlying the East Sulawesi Ophiolite (ESO), Indonesia using an improved chemical separation protocol tailored to these environments. In addition to the analytical refinements introduced, this study aims to (1) provide a better understanding of the process and environmental conditions that influence the mobility of Mo during intense tropical weathering of ultramafic bedrock and (2) evaluate its significance in the overall Mo flux to the riverine and ocean systems in these settings.

2. Study site

The K-shaped island of Sulawesi is located at the triple junction of the Australian, Pacific, and Eurasian tectonic plates, and is composed of four elongated arms that broadly represent different lithotectonic domains (Fig. 1a, Hall and Wilson, 2000; Hamilton, 1973; Katili, 1978). The study site is located in the central-southeastern part of the island, which is primarily composed of ophiolite bedrock successions of the East Sulawesi Ophiolite (ESO; Fig. 1), one of the three largest ophiolite complexes in the world (Kadarusman et al., 2004; Parkinson, 1998). The emplacement of the ESO took place during the Late Mesozoic according to paleomagnetic data (~137 Ma; Mubroto et al., 1994). During a phase of collision and accretion of island arcs and oceanic crust on the Eurasian margin, the highly tectonized ESO was obducted around 30–40 Ma ago (Kadarusman et al., 2004; Monnier et al., 1995). The ESO comprises ultramafic mantle rocks (lherzolites and harzburgites), cumulate gabbro, sheeted dolerites, and basalts of normal mid-ocean ridge basalt (MORB) composition (Fig. 1b; Kadarusman et al., 2004; Villeneuve et al., 2002). Owing to the tropical climate, with average temperatures of 26 °C and annual rainfall averaging 2700 mm in the region (Aldrian and Dwi Susanto, 2003; Costa et al., 2015; Hendon, 2003; Kurniadi et al., 2021), the ESO is intensely weathered and overlain by thick lateritic weathering profiles (Fig. 1c; Morlock et al., 2019). Laterite profiles studied here were accessed in the catchment of the Malili Lake system, comprising the larger lakes Matano, Mahalona, and Towuti (Morlock et al., 2019; Fig.1b).

3. Materials and methods

A total of twenty samples were collected from different, visually discernible, weathering horizons in six different laterite profiles (Fig. 1b, c; hereafter: laterite samples). In addition, six ultramafic bedrock samples from the bedrock underlying the weathering profiles were collected (Table 1). The weathering profiles vary in thickness between 2 and 8 m and consist of dark red laterite, red laterite, yellow laterite, and saprolite zones, essentially following a characteristic geochemical and mineralogical zonation of well-developed tropical laterites (Fig. 1c; Morlock et al., 2019). For clarity, sample IDs are renamed here following their profile ID and zonation, compared to previous studies that utilized the same set of samples (Table 1; Morlock et al., 2019). Profile 6 is the most representative in terms of sample coverage and shows the best-developed lateritic weathering zonation (Fig. 1c). Profiles 2, 3, and 4 overlie serpentinized peridotite whereas profiles 1, 5, and 6 overlie peridotite bedrock (Morlock et al., 2019).

Prior to analysis, laterite samples were freeze-dried and homogenized/ground to a fine powder using an agate mortar and pestle. Bedrock samples were placed into an aramid mesh to avoid contamination and crushed using a hammer to a grain size of <2 mm. These were subsequently milled to a fine homogeneous powder using an agate

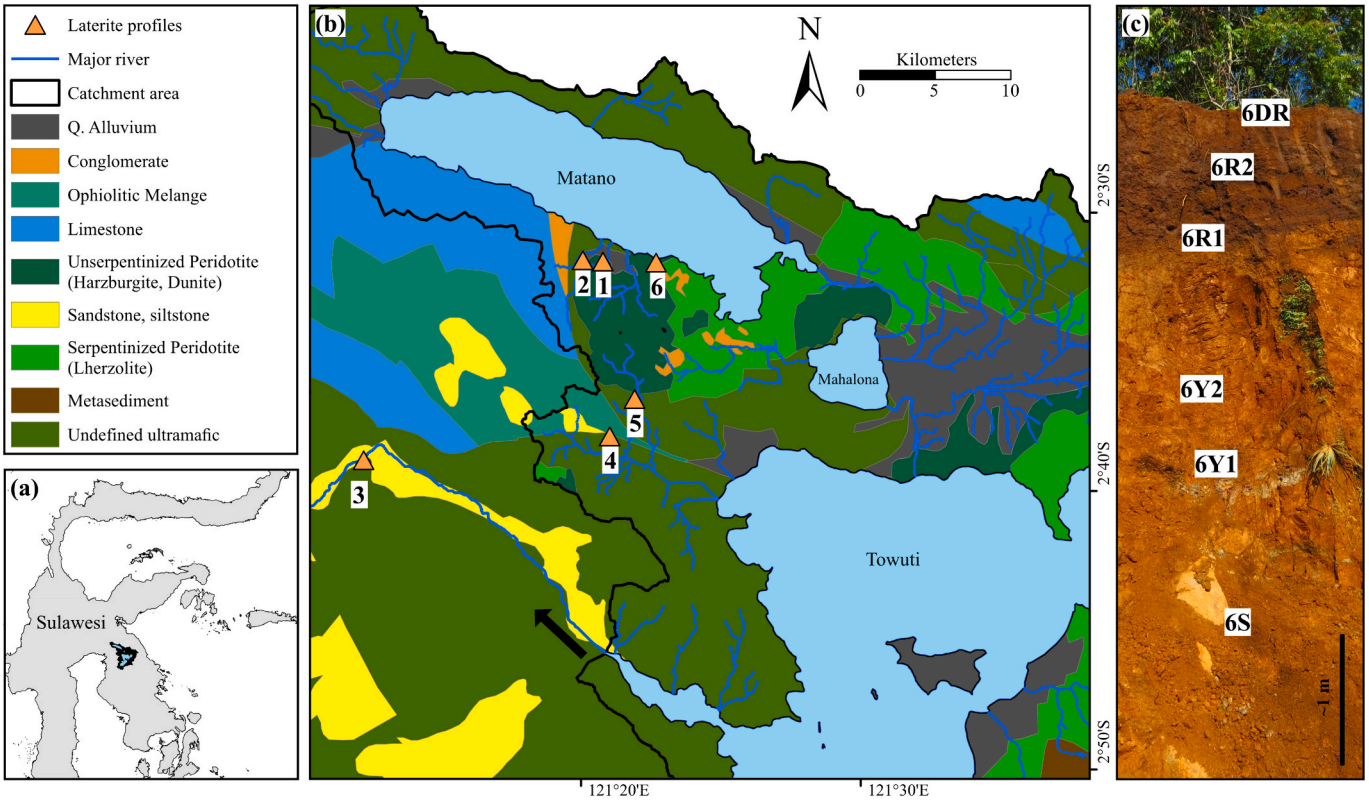

Fig. 1. (a) Sulawesi island (b) Geological map (modified from Costa et al., 2015) of laterite profile sampling points plotted in black triangles. The catchment area of the Malili Lake System (Morlock et al., 2019) is indicated as the black line. Black arrow indicates the outflow of Lake Towuti. (c) Field photographs of Profile 6.

planetary mill set to 600 rpm for ~10 min.

3.1. Major and trace element measurement

Major and trace element concentration data used here were previously published by Morlock et al. (2019). The major and trace element measurements were performed using inductively coupled plasma mass spectrometry (ICP-MS) following full acid digestion (HF, HCl, HNO_3, and $HClO_4$) of 0.5 g of fine ground samples at the Activation Laboratories Ltd. in Ontario, Canada. Due to the detection limit being reached for some elements, samples were also measured with wavelength dispersive X-ray fluorescence (WD-XRF; Morlock et al., 2019). Due to the expected low Mo concentration in laterite and bedrock samples, Mo concentrations were obtained by the isotope dilution method using the double-spike deconvolution of Mo isotope measurement used here (see subsection 3.4).

3.2. Total organic carbon measurement

Total carbon (TC), total nitrogen (TN), and total sulfur (TS) were measured by flash combustion elemental analysis using a Thermo Fisher Elemental Analyzer at the Institute of Geological Sciences, University of Bern. Around 5 to 8 mg of dried and powdered laterite samples were weighed into tin capsules. For total organic carbon (TOC) measurements, around 4 to 5 mg of dried and powdered samples were weighed into silver capsules and dropwise treated with 1 M HCl until all carbonate was dissolved. Subsequently, samples were dried in an oven for 48 hours at 40 °C. Samples in both tin and silver capsules were flash-combusted at 1300 °C with the addition of O_2 during combustion, gases were chromatographically separated and quantified by means of a thermal conductivity detector. The detection limits are 0.01, 0.02, and 0.05 wt% for TN, TC, and TS, respectively.

3.3. Calculation of degree of weathering

The mafic index of alteration (MIA) and the index of laterization (IOL) were calculated for each sample in this study, to better quantify chemical exchange during the weathering of mafic bedrock compared to the published chemical index of alteration (CIA; Morlock et al., 2019). Although Babechuk et al. (2014) suggest that the MIA is only suitable for incipient to intermediate weathering and the IOL is preferred for high-intensity weathering regimes, both MIA and IOL are examined in this study due to the large range of weathering degrees throughout the profiles. MIA and IOL were calculated from oxide concentrations measured by WD-XRF (Morlock et al., 2019). The MIA is based on the net loss of the mobile major elements (CaO, MgO, Na_2O, and K_2O) relative to the immobile major elements (Al_2O_3 and Fe_2O_3) whereas the IOL is based on the ratio of SiO_2 relative to $Al_2O_3 + Fe_2O_3$. The IOL is displayed alongside the ternary diagram of SAF (SiO_2 vs. Al_2O_3 vs. Fe_2O_3) with the 'limit of kaolinization' being indicative for the early to intermediate stages of weathering assuming that all the Al available in the protolith is first converted to kaolinite, and that further weathering beyond these conditions marks the onset laterization (Babechuk et al., 2014; Widdowson, 2007). The limit of kaolinization and further group division for laterization were calculated based on sample 4B which is the bedrock with the highest Al_2O_3 (Table S1).

3.4. Mo purification and isotope measurement

Molybdenum purification and isotope analysis were performed at the clean laboratory and mass spectrometry facilities of the Institute of Geological Sciences, University of Bern. Between 40 and 4440 mg of homogenized samples were weighed into pre-cleaned 15 or 60 mL Savillex™ Teflon beakers to obtain 25 to 50 ng of Mo. Samples were spiked with an appropriate amount of isotope tracer solution enriched in ^{97}Mo and ^{100}Mo (Siebert et al., 2001). Digestion and chemical

Table 1
[Mo], δ^{98}Mo, and other relevant parameters. Trace elements are from Morlock et al. (2019).

Sample ID (Morlock et al., 2018)	Sample ID (this study)	Profile No	Zone	Profile Depth	[Mo] (μg. g^{-1})	δ^{98}Mo (‰)	2SE (‰)	Fe_2O_3 (%)	TOC (%)	Sc (μg. g^{-1})	Ti (%)	Zr (μg. g^{-1})	τMo_{Sc}	τMo_{Ti}	τMo_{Zr}	τMo	τFe	$\Delta^{98}Mo_{laterite-bedrock}$ (‰)	MIA (%)	IOL (%)
LAT2	1DR	1	dark red horizon	0.4	0.53	−0.009*	0.020	56.2	0.36	67	0.061	13	5.05	2.88	1.60	2.88	−0.36	0.104	87	81
LAT3	1Y2	1	yellow horizon	1	0.15	−0.069*	0.030	59.0	0.12	66	0.047	7.9	0.74	0.42	0.21	0.42	−0.08	0.043	98	77
LAT4	1Y1	1	yellow horizon	1.5	0.51	−0.052*	0.020	68.3	0.05	86	0.095	24.8	3.54	1.40	0.31	1.40	−0.53	0.061	99	92
Weathered BED8	1WB	1	weathered bedrock	8	0.014	−0.20**	0.022	10.0	0.05	12	0.007	0.9	−0.13	−0.13	−0.03	−0.13	0.14	−0.089	20	20
BED8	1B	1	bedrock	8	0.016	−0.11**	0.035	9.0		12	0.007	1	0.00	0.00	0.00	0.00	0.00	0.000	18	18
LAT6a	2DR	2	dark red horizon	0.1	0.21	0.13**	0.014	68.9	0.58	39	0.137	10.7	0.09	−0.69	0.06	0.06	−0.50	−1.234	99	94
LAT6b	2R	2	red horizon	2	0.10	0.11**	0.013	71.0	0.46	40	0.108	6.6	−0.46	−0.80	−0.14	−0.46	−0.34	−1.252	98	94
SAP3	2S	2	saprolite	2.5	0.030	0.62** 0.56**	0.017	11.1	0.46	16	0.045	1.7	−0.62	−0.86	−0.05	−0.62	−0.74	−0.737	25	22
BED9	2B	2	bedrock	3.5	0.015	1.36**	0.020	8.8		3	0.003	0.8	0.00	0.00	0.00	0.00	0.00	0.000	20	18
LAT7a	3DR	3	dark red horizon	0.3	0.030	−0.36**	0.014	18.0	0.29	27	0.106	10.8	1.20	−0.59	−0.45	−0.45	−0.55	−0.303	55	33
LAT7b	3Y	3	yellow horizon	1	0.025	−0.44**	0.016	22.4	0.33	27	0.047	4.2	0.82	−0.24	0.17	0.17	−0.20	−0.382	61	37
BED12	3B	3	bedrock	8	0.006	−0.053**	0.019	7.9		11	0.008	1.1	0.00	0.00	0.00	0.00	0.00	0.000	18	18
LAT8c	4DR	4	dark red horizon	0.05	0.087	0.090**	0.014	24.6	3.04	31	0.22	13.7	1.60	1.12	1.41	1.41	0.45	0.424	76	49
LAT8a	4R	4	red horizon	0.4	0.19	−0.090**	0.016	29.9	1.32	33	0.148	13	4.27	5.81	4.49	4.49	1.01	0.244	75	54
LAT8b	4Y	4	yellow horizon	1.2	0.036	0.027**	0.016	30.9	1.01	37	0.17	11.9	−0.09	0.14	0.16	0.14	0.97	0.361	87	49
BED15	4B	4	bedrock	15	0.021	−0.33**	0.016	9.5		19	0.11	7.8	0.00	0.00	0.00	0.00	0.00	0.000	32	29
LAT9a	5DR	5	dark red horizon	0.2	0.58	0.12**	0.014	71.6	0.95	68	0.111	29.9	5.78	8.86	2.17	5.78	0.30	0.285	99	98
LAT9b	5R	5	red horizon	1.5	0.19	0.075**	0.014	73.7	0.39	68	0.062	18.9	1.21	4.75	0.63	1.21	0.99	0.241	99	98
LAT9c	5Y	5	yellow horizon	2.5	0.19	0.060**	0.018	73.7	0.65	59	0.059	11.6	1.59	5.15	1.70	1.70	1.34	0.227	99	98
Estimated BED	5 EB	5	bedrock	4	0.014	−0.17**		8.82		11.2	0.027	2.3	0.00	0.00	0.00	0.00	0.00	0.000	21	21
LAT10a	6DR	6	dark red horizon	0.1	0.29	−0.13* −0.056**	0.017	51.6	0.22	26	0.067	10.8	6.88	0.39	0.38	0.39	0.11	0.035	96	86
LAT10b	6R2	6	red horizon	1	0.24	−0.16*	0.020	55.6	0.10	33	0.068	10	4.18	0.14	0.24	0.24	0.02	0.005	95	91
LAT10c	6R1	6	red horizon	1.5	0.32	−0.092*	0.017	52.4	0.24	36	0.077	11.8	5.41	0.36	0.42	0.42	−0.14	0.074	93	92
LAT10d	6Y2	6	yellow horizon	2.5	0.022	−0.47***	0.032	61.2	0.18	37	0.043	4.1	−0.58	−0.84	−0.73	−0.73	0.40	−0.306	95	88
LAT10f	6Y1	6	yellow horizon	3	0.048	−1.03***	0.024	21.9	0.12	24	0.05	6.3	0.43	−0.69	−0.60	−0.60	−0.43	−0.861	66	33
LAT10e	6S	6	saprolite	3.5	0.037	−0.78***	0.031	38.4	0.07	45	0.082	9.6	−0.42	−0.85	−0.80	−0.80	−0.44	−0.618	81	55
BED18	6B	6	bedrock	4	0.015	−0.17**	0.015	8.9		11	0.005	0.8	0.00	0.00	0.00	0.00	0.00	0.000	17	18

* Mo purification and isotope analysis were performed with the standard procedure explained in the Mo isotope measurement subsection.
** Mo purification and isotope analysis were performed with the modified procedure explained in Supplementary Material.
*** Mo purification and isotope analysis were performed with the modified procedure explained in Supplementary Material. These samples had high δ^{98}Mo correction due to Ru interference (up to 0.95‰) and procedural blank correction (2.4 ng; ~10% of total Mo).

separation processes for the samples from batch 1 were done with the standard procedure, whereas a modified digestion and Mo purification protocol was applied for samples from batch 2, 3, and 4 (Table S2). For the standard procedure, samples were dissolved in a concentrated single distilled 3:1 mixture of HF and HNO_3 for at least 48 h for all samples at 100 °C. Solid residuals were treated with 14 M HNO_3 for at least 48 hours before 6 M HCl was added at least twice. During the dissolution in HNO_3 and HCl, the beakers were placed on a hotplate at 80 °C and 120 °C, respectively. Subsequently, samples were purified using a sequence of anion and cation exchange resin. All the standard chemical separations were performed following procedures reported earlier (Ahmad et al., 2021; Wille et al., 2013). In brief, samples were dissolved in 3 mL 4 M HCl + 0.15% H_2O_2 before being loaded into a single column with 2 mL anion exchange resin Dowex® AG 1 × 8 (200–400 mesh) for chemical separation. For further chemical separation, samples were prepared in 2 mL 0.5 M HCl + 0.1% H_2O_2 before being loaded into a single column with 2 mL cation exchange resin Dowex® 50 × 8 (200–400 mesh).

Where a high amount of sample material was needed due to low Mo concentrations, the separation procedure was modified to minimize the effect of Fe and Ru on the chemical separation procedure and isobaric inferences during analysis, respectively. Accordingly, Cr^{6+} was added to oxidize Ru which subsequently evaporated (Hopp et al., 2016). Excess Cr^{6+} was reduced with HAsc (Ascorbic Acid; $C_6H_8O_6$) and underwent additional Mo purification (Larsen et al., 2016; Xu et al., 2004). Furthermore, HAsc was added to reduce Fe^{3+} to Fe^{2+} prior to loading the sample solution onto the anion exchange resin (Willbold et al., 2016) to prevent oversaturation of the resin with Fe^{3+}. Details of the modified protocol are described in Supplementary Material.

Ultimately, samples were dissolved in 1.2 mL 0.5 M HNO_3 for measurement by a NeptunePlus multicollector inductively coupled plasma mass spectrometer (MC-ICP-MS) coupled to an Aridus II desolvating nebulizer. Six Mo isotopes (^{94}Mo, ^{95}Mo, ^{96}Mo, ^{97}Mo, ^{98}Mo, and ^{100}Mo) were measured as well as ^{99}Ru and ^{101}Ru to monitor isobaric interference. We used faraday cups with 10^{11} Ω amplifiers to analyze all isotopes except ^{101}Ru, which was measured using a 10^{12} Ω amplifier. For analyses, we have used a combination of the standard 'H' Ni sampler cone and the 'X' Ni skimmer cone and obtained ~64 V/ppm on ^{95}Mo. Mo isotope ratios are reported as parts per thousand deviations of ^{98}Mo/^{95}Mo of the sample relative to NIST SRM 3134 = 0‰. Where necessary, published Mo isotope data reported in this study have been recalculated to NIST SRM 3134 = 0‰. Mo isotope ratios were calculated using the double-spike correction method (Siebert et al., 2001) with an interference correction based on simultaneously measured ^{99}Ru. Repeated measurement of the in-house Johnson Matthey standard solution lot 602332B ("JMCBern"; Siebert et al., 2001) gave an isotopic difference of 0.26 ± 0.01‰ δ^{98}Mo (2SD; n = 19) relative to NIST SRM 3134 (Goldberg et al., 2013; Greber et al., 2012) in agreement with previous studies (Ahmad et al., 2021; Ahmad et al., 2022, 2023; Greber et al., 2012; Kaufmann et al., 2021; O'Sullivan et al., 2021, 2022). Background correction was applied by averaging background intensities of pure 0.5 M HNO_3 carrier solution that was measured on-peak before and after the analysis of every sample. Sample and background analysis consisted of 80 and 30 cycles, respectively, with a signal integration time of 4.194 s for each cycle. The Mo blanks of the chemical procedures are presented in Table S2. Mo isotope composition of samples with ~10% of blanks contribution (6Y2, 6Y1, 6S) was corrected using the Mo isotope composition of the full procedural blanks. Analyses of individually digested and chemically purified AGV-2, BHVO-2, BIR-1a, and W-2a whole-rock reference materials yielded δ^{98}Mo of −0.18 ± 0.01‰ (2SD; n = 4), −0.06 ± 0.02‰ (2SE; n = 1), −0.13 ± 0.02‰ (2SE; n = 1), and − 0.03 ± 0.06‰ (2SD; n = 3), respectively. These values are in agreement with previously published values (Fan et al., 2020; Feng et al., 2020; Willbold et al., 2016; Zhao et al., 2016). Individual measurements of geological whole-rock reference materials and blank measurements can be found in Table S3. We consider ±0.06‰ the long-term 2 SD reproducibility of the sample measurements as determined by the measurement of W-2a. This is in line with previous measurements of BHVO-2 (−0.09 ± 0.05‰; 2SD; n = 11) done at the Institute of Geological Sciences, University of Bern (Ahmad et al., 2021; Ahmad et al., 2022, 2023). Additionally, some samples were double-measured after individual sample digestion and chemical separation, and showed agreement (Table 1, Table S2).

3.5. Calculation of elemental loss and gain and Mo isotopic deviation

The Mo losses and gains were calculated relative to immobile elements using the following equation (Nesbitt and Young, 1982):

$$\tau Mo_{im} = \frac{\left(\frac{C_{Mo}}{C_{im}}\right)_l}{\left(\frac{C_{Mo}}{C_{im}}\right)_b} - 1$$

where C_{Mo} and C_{im} are the concentrations of Mo and immobile elements, respectively, while l and b refer to samples and the bedrock, respectively. Due to the limit of detection of ICP-MS and relatively low contents of some commonly used immobile elements e.g. Nb, Th, and Hf in some of the samples, we use Sc, Ti, and Zr in the calculations. The median of Mo loss and gain relative to each immobile element (τMo_{Sc}, τMo_{Ti}, τMo_{Zr}) were used to exclude the value that deviates significantly from the others, expressed as the Mo loss and gain (τMo). Positive and negative τMo values indicate that Mo experienced either gain or loss, respectively, relative to the immobile element employed. The same calculations were applied to calculate the losses and gains of Fe in the weathering profiles (τFe). The $\Delta^{98}Mo_{laterite\text{-}bedrock}$ (‰) of each laterite sample was calculated relative to its respective bedrock δ^{98}Mo to indicate the Mo isotope deviation of each soil sample. Given that we lack a bedrock sample for profile 5, we used averaged element concentration and δ^{98}Mo of bedrock samples from profiles 1, 3, 4, and 6 to calculate the τMo and $\Delta^{98}Mo_{laterite\text{-}bedrock}$ for profile 5.

4. Results

4.1. Degree of weathering

The MIA values are in general agreement with IOL showing large coverage in the extent of the weathering process (Fig. 2a). The IOL is displayed alongside the SAF (SiO_2 vs. Al_2O_3 vs. Fe_2O_3; Fig. 2b; Babechuk et al., 2014) while the MIA for all samples is displayed in the AF-CNK-M ($Al_2O_3 + Fe_2O_3$ vs. CaO + Na_2O + K_2O + vs. MgO) diagram (Fig. S1) to illustrate the weathering trends and intensity in the weathering profiles. The IOL variation of all the samples in the SAF diagram (Fig. 2b) suggests that each profile shows a somewhat different degree of laterization as a result of a slight difference in site characteristics (slope angle, vegetation cover, profile thickness etc.) and a sampling strategy that targeted horizons distinct in color. Nevertheless, all samples follow a similar trend of changing major element concentrations during laterization. This is expected due to the similar bedrock compositions and the same weathering regime for all profiles.

The limit of kaolinization calculated from sample 4B is 56.5% SiO_2 or 43.5% in IOL. All bedrock samples show a low IOL (<30%). Furthermore, based on the calculation of the extent of weathering/laterization (Table S1), samples are divided into 5 groups (Fig. 2): (1) bedrock and weathered bedrock samples with IOL <30%, (2) kaolinized samples with IOL = 30–44%, (3) weakly-laterized samples with IOL = 44–62%, (4) moderately-laterized samples with IOL = 62–81%, and (5) strongly-laterized samples with IOL = 81–100% (Fig. 2). Additionally, considering the highest IOL and MIA for the samples from profile 5 with 99% and 98%, respectively, these samples can be separated from group 5 making it into group 5a and group 5b (Fig. 2a). Profile 6 as the most representative profile in terms of sample coverage shows the most

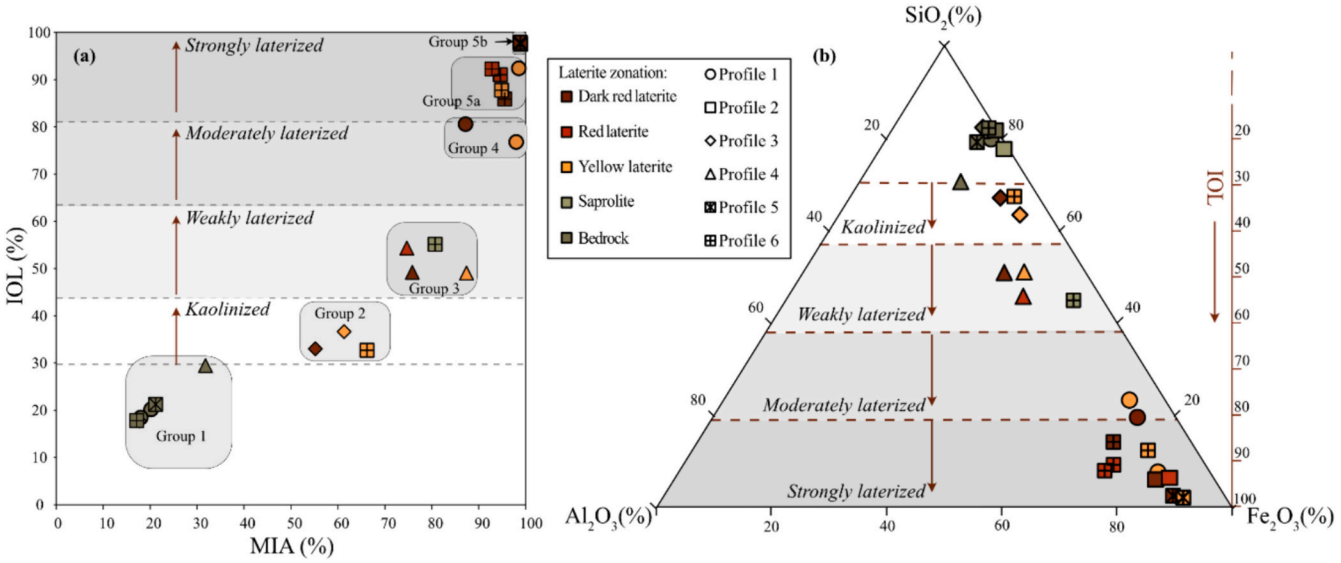

Fig. 2. (a) The mafic index of alteration (MIA) (%) vs. index of laterization (IOL) (%) and sample grouping. (b) SAF (SiO_2 (%) vs. Al_2O_3 (%) vs. Fe_2O_3 (%)) ternary diagram. The IOL (%) is shown as a vertical line with higher values indicating stronger weathering.

variable degree of laterization among profiles (Table 1).

4.2. [Mo] and δ^{98}Mo variability

The Mo concentration ([Mo]), δ^{98}Mo, and all other parameters i.e. Fe_2O_3, TOC, Sc, Ti, Zr, τMo_{Sc}, τMo_{Ti}, τMo_{Zr}, τMo, τFe, $\Delta^{98}Mo_{laterite\text{-}bedrock}$, MIA, and IOL are listed in Table 1. The [Mo] of each sample are presented in Fig. 3a. The [Mo] of laterite samples is generally higher (0.022 to 0.58 $\mu g \cdot g^{-1}$) compared to those in bedrock samples (0.006 to 0.021 $\mu g \cdot g^{-1}$). These results are in line with those previously reported for soils (King et al., 2016; Liu et al., 2020; Siebert et al., 2015; Wang et al., 2018) and peridotite (Liang et al., 2017; Wang and Becker, 2018), respectively. While all laterite samples from the topmost red and dark red laterite horizons show the most Mo enrichment relative to the underlying bedrock, Mo enrichment factors are very variable ranging from 41.1 to 4.2 in profiles 5 and 4, respectively.

The δ^{98}Mo of each sample are presented in Fig. 3b. Except for the bedrock in profile 2, the δ^{98}Mo composition of the peridotite bedrock samples, including one weathered bedrock (1WB), ranges from −0.05‰ to −0.33 ‰ (−0.17 ± 0.24‰ δ^{98}Mo; 2SD; $n = 5$). The bedrock in profile 2 shows a substantially higher δ^{98}Mo value of 1.36‰ indicating serpentinization. Although interaction with seawater cannot be excluded for the bedrock of all profiles (Morlock et al., 2019), the high δ^{98}Mo of the bedrock of profile 2 shows agreement with previously reported δ^{98}Mo of serpentinized mafic rocks retaining the heavy Mo isotopic composition of seawater during alteration (Chen et al., 2019; Dai et al., 2024; Rojas-Kolomiets et al., 2023). The δ^{98}Mo of laterite samples varies from +0.12 to −1.03‰ (−0.20 ± 0.65‰ 2SD; $n = 17$) and +0.29 ± 0.59‰ (2SD; $n = 3$) for the profile overlying peridotite and serpentinized peridotite, respectively.

4.3. Mo- loss and gain

Overall, the τMo values vary from −0.80 to +5.77 (Table 1; Fig. 4). Except for profile 2, all profiles show a general trend of Mo gain in the topmost red and dark red laterite zones. Conversely, weathered bedrock and laterite samples from the lower saprolite zone show a loss of Mo while samples from the intermediate yellow laterite zones show both loss and gain.

4.4. Total organic carbon

The TOC in all the laterite samples varies from 0.03 to 3.04%, averaging 0.48% (Table 1). All samples of profile 4 have a comparatively higher TOC concentration with an average of 1.8% than samples of other profiles.

5. Discussion

5.1. Mo concentration and isotope variability in the lateritic weathering profile overlying ultramafic bedrock

In-field laterite zonation of each profile is not precisely in agreement with the weathering degree indices (MIA or IOL; Fig. 2). Therefore, we compare changes in the [Mo] and τMo to IOL, with its respective groupings (Fig. 5). Excluding profile 4, with high OM content, most of the kaolinized and weakly-laterized samples (Groups 2 and 3), with an IOL of up to 62%, show low [Mo], and negative τMo except for sample 3Y (Fig. 5). This possibly indicates aqueous mobility and loss of Mo from these laterite zones during the early stages of laterization. In contrast, moderately- and strongly-laterized zones (Groups 4 and 5) show generally high [Mo], and substantial Mo gain, originating from internal and/or possibly external sources (Fig. 5). Sample 6Y2 and samples from profile 2 overlying serpentinized peridotite are exceptions, showing a general loss of Mo despite originating from highly weathered zones (Fig. 5b). Overall, these findings suggest a causal relationship between the different degrees of laterization and the aqueous mobility of Mo within the different profiles.

Accordingly, we calculate τMo and δ^{98}Mo averages of samples from similar degrees of laterization across all the profiles, in order to assess the characteristic behavior of Mo in this setting (Fig. 6). Profile 2, overlying serpentinized bedrock, is discussed separately due to the distinct differences in bedrock type and δ^{98}Mo composition. Excluding profile 4, a general loss of Mo in kaolinized and weakly-laterized samples is accompanied by a shift in δ^{98}Mo towards lower values relative to the bedrock composition (Fig. 6). This can be explained by a) preferential dissolution of less-resistant minerals containing a higher δ^{98}Mo signature compared to bulk Mo and/or b) partial re-adsorption of isotopically light Mo onto secondary minerals. Previous studies have shown that pyroxene can potentially host Mo with a high δ^{98}Mo signature compared to isotopically light Fe-Ti oxides common in mafic bedrock (Wang et al., 2020). Therefore, preferential leaching of

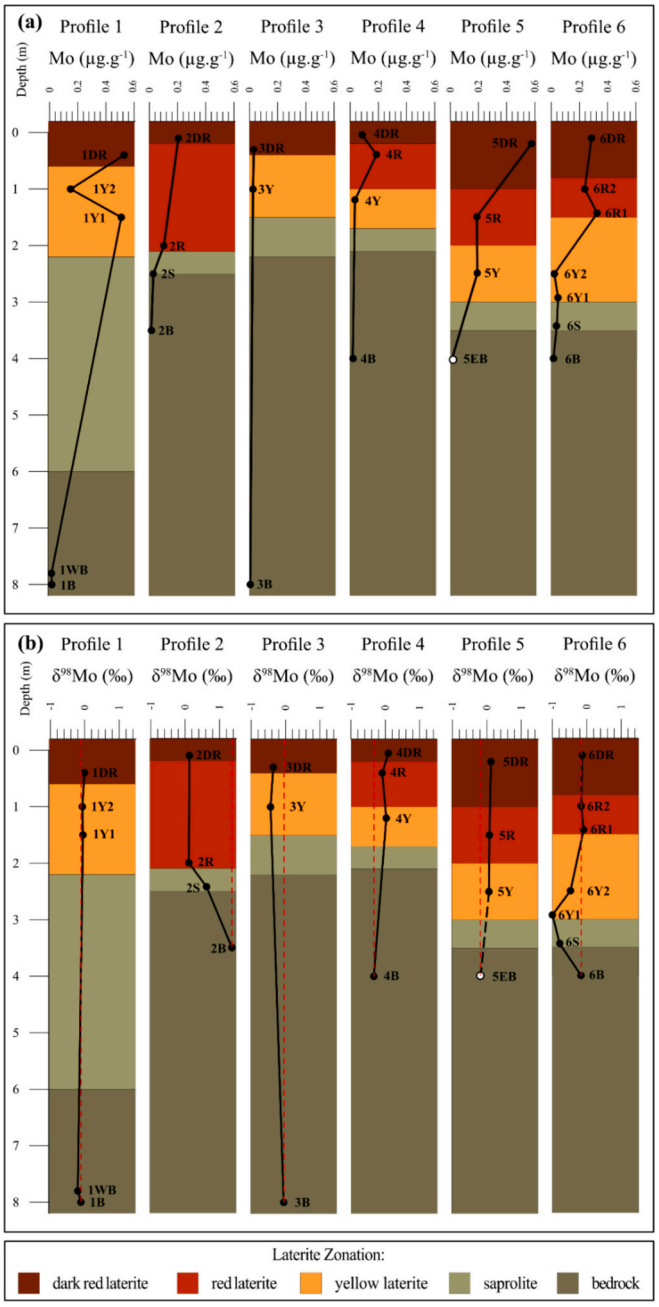

Fig. 3. (a) [Mo] ($\mu g.g^{-1}$) and (b) δ^{98}Mo (‰) variation as a function of depth in the laterite profiles. The red dashed line in (b) indicates δ^{98}Mo of bedrock from the respective profile. The 2SD of δ^{98}Mo in each sample is smaller than the circle icons.

pyroxene minerals in the weakly laterized zone along with the partial re-adsorption of isotopically light Mo onto secondary minerals such as Fe (oxyhydr)oxides, can explain the shift towards low δ^{98}Mo in this lateritic zone. This is in line with previous studies of soils (i.e. Greaney et al., 2021; Siebert et al., 2015; Wang et al., 2018, 2020) and batch experiments (Barling and Anbar, 2004; Goldberg et al., 1996; Goldberg et al., 2009) where (oxyhydr)oxides have been shown to preferentially adsorb light Mo isotopes. Consequently, the δ^{98}Mo profiles reflect the loss and relocation of isotopically heavy Mo fraction by fluids, in line with the negative τMo for the weakly-laterized samples. We suggest that the isotopically heavy Mo fraction is potentially re-scavenged in the more intensely weathered horizons of the laterite profiles, as shown by higher [Mo] and the heavy Mo isotope composition in those horizons (Fig. 6).

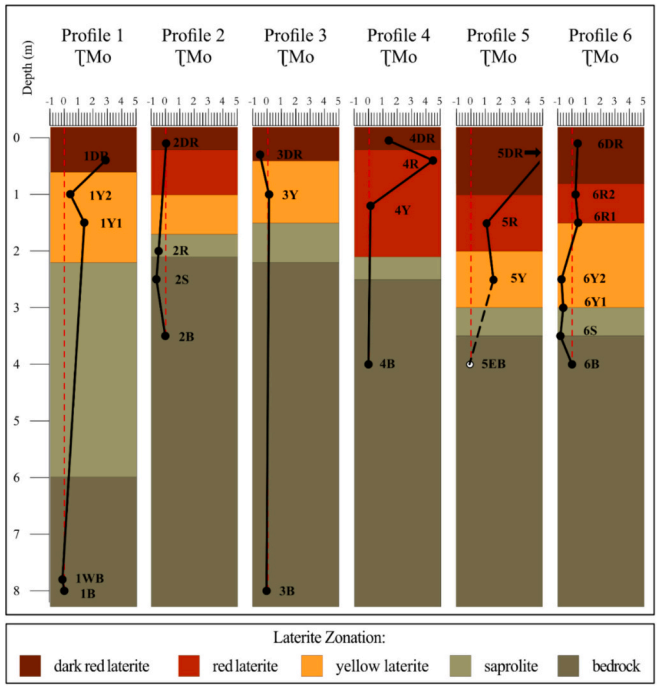

Fig. 4. τMo variation as a function of depth in laterite profiles. The red line indicates zero Mo loss or gain for each profile. Negative values represent Mo loss and positive values Mo gain.

Although regression coefficients between τMo and Fe_2O_3 and TOC concentrations are low, higher τMo are generally associated with samples with high Fe_2O_3 and/or TOC concentrations. Particularly strongly-laterized samples, characterized by the highest τFe (Table 1), exhibit the most positive τMo value (Fig. 6a). Although the rapid decomposition of OM under tropical climatic conditions could mask the relationship between [Mo] and TOC, samples of profile 4 have high TOC concentrations and show a high Mo gain, with τMo up to +4.49, despite the IOL being <62% (Table 1; Fig. 5, 6). This suggests that the formation and abundance of Fe (oxyhydr)oxides during weathering and the availability of OM play important roles in the mobility of aqueous Mo, consistent with previous studies showing that Mo can be effectively scavenged by OM (King et al., 2016; Siebert et al., 2015).

The overall patterns of loss or gain of Mo associated with negative or positive $\Delta^{98}Mo_{laterite\text{-}bedrock}$ values, respectively, suggest a redistribution of Mo within the weathering profile (Fig. 7). The overall low $\Delta^{98}Mo_{laterite\text{-}bedrock}$ in the strongly-laterized samples is likely a result of the overall very low Mo/Fe ratio in this ultramafic setting and ubiquitous Fe (oxyhydr)oxides. Hence, near-complete scavenging of the dissolved Mo pool onto Fe (oxyhydr)oxides may render isotopic fractionation negligible for bulk Mo isotope composition. This is exemplified by the concentration-weighted average δ^{98}Mo of all soil samples of −0.05‰ (n = 17). This δ^{98}Mo composition overlaps, or is slightly higher than but very close to, that of the average peridotite bedrock δ^{98}Mo of −0.17‰ ± 0.21‰ (2SD; n = 5), indicating that the primary mantle-like Mo isotopic composition is retained within the profile during complete weathering. However, in light of the overall higher δ^{98}Mo particularly for strongly-laterized samples, additional external sources with high δ^{98}Mo such as atmospheric input (sea spray, volcanic emissions and fossil fuel combustion) and/or groundwater input (Chappaz et al., 2012; Harkness et al., 2016; King et al., 2016; Liu et al., 2020; Siebert et al., 2015), cannot be entirely excluded.

Local patches of more seawater-altered serpentinized peridotites occur (profile 2) and may also act as an additional source of isotopically heavy Mo. Profile 2 comprises 3 laterite samples with an up-profile IOL sequence of 22%, 94%, and 94%, respectively, lacking kaolinized and

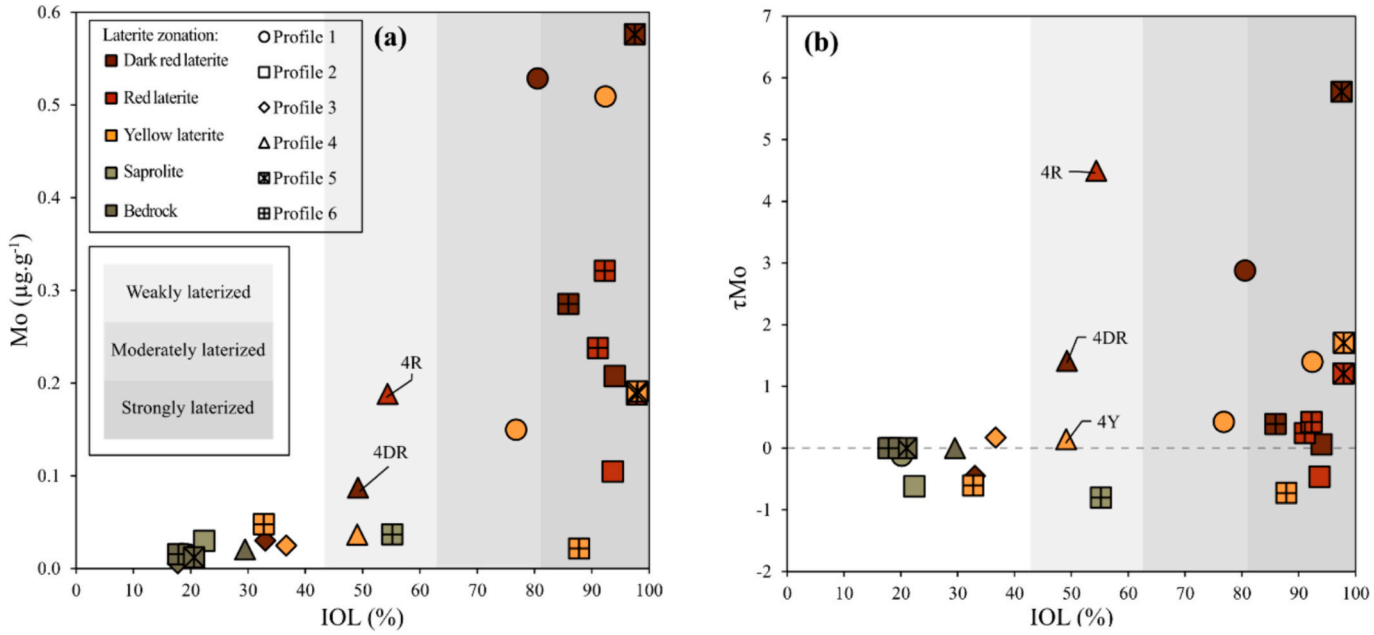

Fig. 5. (a) [Mo] (µg.g^{-1}) and (b) τMo vs. IOL (%). Note that the legends in (a) also apply in (b).

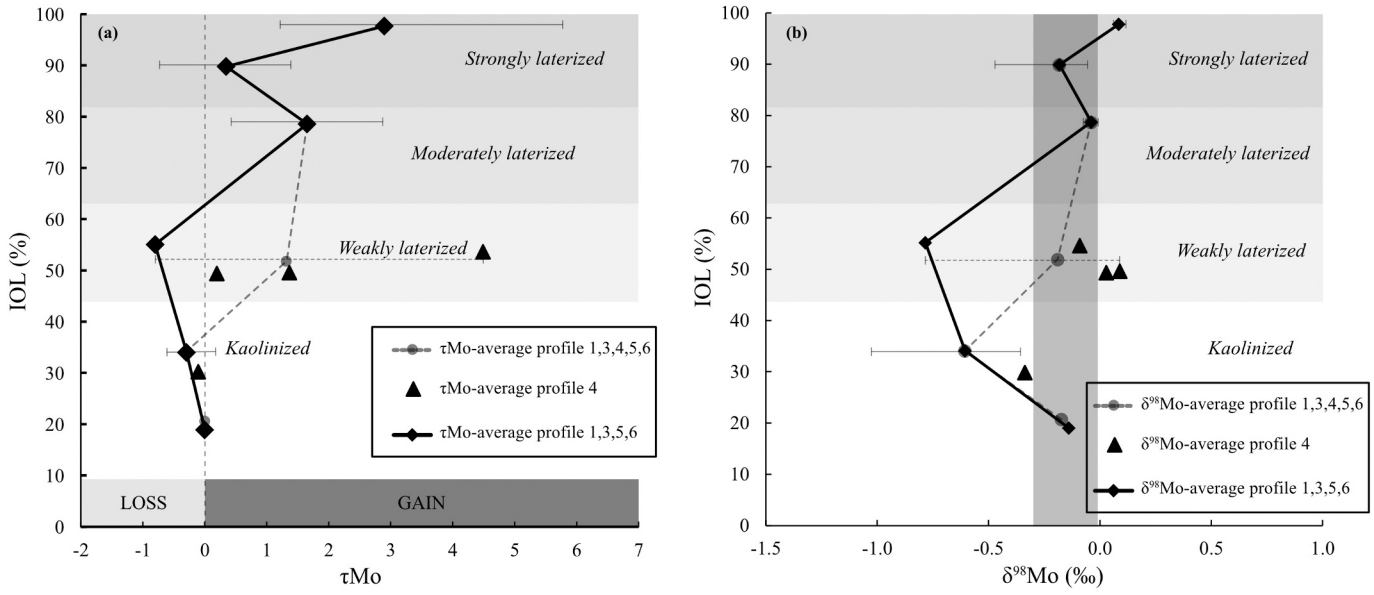

Fig. 6. (a) τMo vs. IOL (%) and (b) δ^{98}Mo (‰) vs. IOL (%) based on the grouping of the IOL (%). The black line indicates the average τMo or δ^{98}Mo of profiles 1, 3, 5, and 6 whereas the dashed line indicates the average if profile 4 is included in the calculation. The error bar indicates the range (max to min) τMo or δ^{98}Mo values.

weakly-laterized samples. The main difference between profile 2 and those profiles overlying unserpentinized peridotite is the inherited heavy Mo isotopic composition of the serpentinized bedrock (+1.36‰ δ^{98}Mo). Contrary to the other profiles, profile 2 shows a trend from initially high δ^{98}Mo bedrock compositions towards low δ^{98}Mo in the most laterized samples. Interestingly, the δ^{98}Mo of the strongly-laterized samples converges towards values which are close to the unserpentinized peridotite bedrock (~0 ‰ to −0.2 ‰; Fig. 3b), associated with a general loss of Mo during weathering indicated by negative τMo values. Although this is in line with the overall observation that isotopically heavy Mo is lost from soil horizons with a low degree of laterization, samples of profile 2, in contrast, show a high degree of laterization. We, therefore, suggest a combination of lateral Mo migration and homogenization during weathering and atmospheric input to explain the observed δ^{98}Mo pattern in profile 2.

5.2. *Comparison of Mo behavior in ultramafic vs. mafic and felsic profiles and its contribution to the Mo riverine composition*

Different weathering regimes and bedrock compositions result in primary minerals with varying susceptibility, which along with changes in the formation of secondary minerals, control the isotopic composition of the soil relative to the respective bedrock. This alters the flux of Mo and its isotopic composition from the weathering profiles into rivers, lakes, and oceans (Greaney et al., 2021; King et al., 2016; Liu et al., 2020; Siebert et al., 2015; Wang et al., 2015, 2018, 2020). Additionally, the availability of OM as an effective Mo scavenger as well as external Mo sources, either natural e.g. seaspray (King et al., 2016; Siebert et al.,

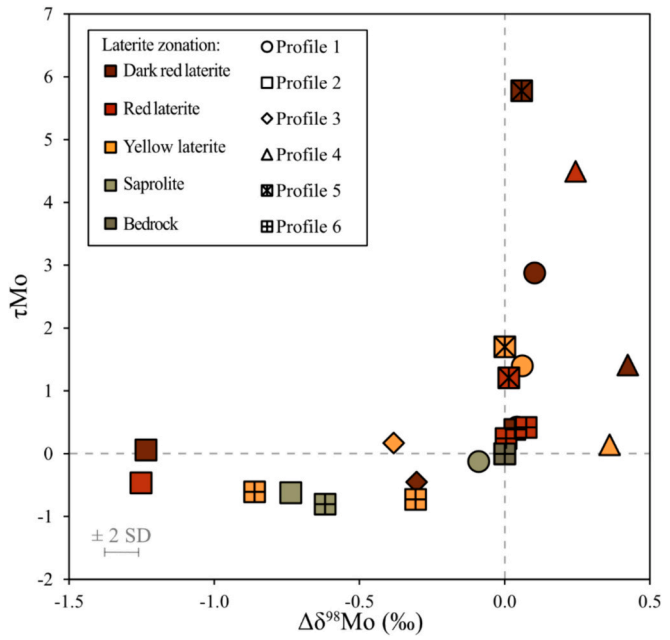

Fig. 7. τMo vs. $\Delta\delta^{98}$Mo (‰) relative to the respective bedrock. The error bar indicates the 2SD long-term reproducibility.

2015) and/or anthropogenic sources (e.g. from fossil fuel combustion; Chappaz et al., 2012; Harkness et al., 2016) may also alter the Mo isotopic composition of soils. Besides the effect of different host minerals, which is not investigated here, all other factors previously discussed are shown to influence the Mo mobility and isotopic composition in lateritic weathering profiles as well. The general trends within the profiles investigated here, with losses and gains of Mo in different weathering zones and associated shifts in isotopic composition (Fig. 8), are in agreement with previous studies (Greaney et al., 2021; King et al., 2016; Siebert et al., 2015; Wang et al., 2018, 2020). However, the low Mo/Fe ratio and ubiquitous Fe (oxyhydr)oxides in the profiles overlying ultramafic bedrock facilitated nearly complete re-scavenging of Mo from the pore water onto weathering products at our study sites.

The formation of saprolite during granite and basalt weathering is connected with an overall loss of heavy Mo relative to the bedrock. These heavy Mo isotope compositions might feed the dissolved Mo reservoirs of rivers and seawater in these settings (Wang et al., 2018, 2020). In contrast, we suggest that lateritic profiles overlying ultramafic bedrock developed under intense tropical weathering are unlikely to have a significant impact on the dissolved Mo budget of the riverine systems and ultimately on the ocean (Fig. 8). Regardless of the high gain (τMo; Fig. 4), the inherited low [Mo] of the bedrock from these ultramafic laterite profiles likely result in an insignificant contribution (Fig. 8a). This is in line with a recent study of Mo in the Amazon River that suggested the control of the weathering regime on Mo release, with higher weathering intensity resulting in a low [Mo] contribution (Revels et al., 2021). This additionally underlines the importance of the transport of Mo, which in ultramafic bedrock-dominated catchments primarily occurs in the form of Fe (oxyhydr)oxide particles. Release of Mo adsorbed onto Fe (oxyhydr)oxides, which are chemically stable under oxic and high pH conditions is restricted, but enhanced in anoxic/reducing and low pH settings. Thus, only the physical transport of suspended Fe (oxyhydr)oxide particles into reducing, redox-stratified aquatic systems and sediments can liberate adsorbed Mo, and potentially other redox-sensitive and particle-reactive elements such as Cr, As, Ni, P, and Co (Hongve, 1997; Koschinsky and Hein, 2003) into the aquatic environment.

6. Conclusion

Analysis of Mo concentration and isotopic composition from tropical weathering profiles overlying ultramafic bedrock shows Mo enrichment in the topmost horizons of the weathering profiles and nearly complete re-scavenging of Mo, primarily by ubiquitous Fe (oxyhydr)oxides. Although Mo redistribution within the soil profile likely leads to the large Mo isotope variability observed in between laterite samples from different depths, the concentration-weighted average δ^{98}Mo of all laterite samples is close to that of the ultramafic bedrock with slightly higher δ^{98}Mo in strongly laterized samples. Owing to the low initial bedrock concentration, atmospheric and/or groundwater input may also contribute to the observed high δ^{98}Mo composition. As a consequence, the Mo transport in rivers draining predominantly ultramafic catchments is dominated by particulate transport of suspended Fe (oxyhydr) oxides. This limits the contribution of dissolved Mo to aqueous Mo budgets from these environments. However, elements such as Mo that

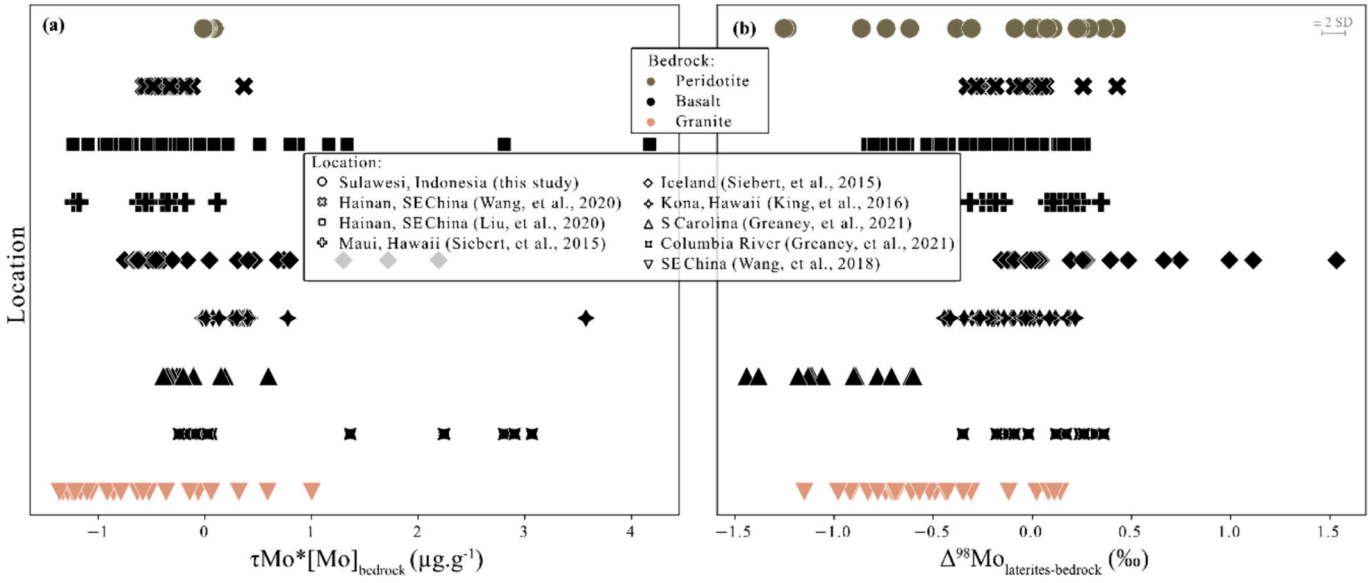

Fig. 8. Comparison of (a) [Mo] ($\mu g.g^{-1}$) as the product to the Mo gain or loss (τMo) and (b) $\Delta^{98}Mo_{laterite\text{-}bedrock}$ (‰) variability, relative to the respective unweathered bedrock from different weathering profiles overlying different bedrocks. The error bar indicates the 2SD long-term reproducibility.

are immobilised by adsorption onto Fe (oxyhydr)oxide can be released in reducing aquatic and sedimentary environments.

CRediT authorship contribution statement

Adrianus Damanik: Writing – review & editing, Writing – original draft, Visualization, Methodology, Investigation, Formal analysis, Data curation. **Martin Wille:** Writing – review & editing, Visualization, Supervision, Methodology, Formal analysis, Data curation, Conceptualization. **Qasid Ahmad:** Writing – review & editing, Methodology, Data curation. **Sukalpa Chatterjee:** Writing – review & editing, Data curation. **Sean A. Crowe:** Writing – review & editing. **Kohen W. Bauer:** Writing – review & editing. **Martin Grosjean:** Writing – review & editing, Supervision. **Sri Yudawati Cahyarini:** Writing – review & editing, Supervision, Funding acquisition. **Satria Bijaksana:** Writing – review & editing. **James M. Russell:** Writing – review & editing, Funding acquisition. **Hendrik Vogel:** Writing – review & editing, Writing – original draft, Supervision, Resources, Project administration, Investigation, Funding acquisition, Conceptualization.

Declaration of competing interest

The authors declare that they have no known competing financial interests or personal relationships that could have appeared to influence the work reported in this paper.

Data availability

Data will be made available on request.

Acknowledgements

This research was carried out with support from the German Research Foundation (DFG) and the Swiss National Science Foundation (SNSF) through grants awarded to H. Vogel (DFG: VO 1591/2-1; SNSF: 200020_188876 & 200021_153053) as well as through the U.S. National Science Foundation (NSF) through grants awarded to J.M. Russell. The MC-ICP-MS at the Institute of Geological Sciences, University of Bern used in this study was acquired within the framework of the NCCR project PlanetS (Grant nr. 1NF40-141881) funded by the SNSF. Foreign research permits for field work at Lake Towuti were kindly granted by the Ministry of Research, Education, and Higher Technology of Indonesia (RISTEK) permit number 02/TKPIPA/FRP/SM/II/2010. Logistical support was kindly provided by PT Vale Indonesia. We also thank Derek Vance, Anthony Chappaz, and 1 anonymous reviewer for constructive reviews, as well as Mary Ayyamperumal and Karen H. Johannesson for editorial handling.

Appendix A. Supplementary data

Supplementary data to this article can be found online at https://doi.org/10.1016/j.chemgeo.2024.122150.

References

Ahmad, Q., Wille, M., König, S., Rosca, C., Hensel, A., Pettke, T., Hermann, J., 2021. The Molybdenum isotope subduction recycling conundrum: a case study from the Tongan subduction zone, Western Alps and Alpine Corsica. Chem. Geol. 576, 120231 https://doi.org/10.1016/j.chemgeo.2021.120231.

Ahmad, Q., Wille, M., Rosca, C., Labidi, J., Schmid, T., Mezger, K., König, S., 2022. Molybdenum isotopes in plume-influenced MORBs reveal recycling of ancient anoxic sediments. Geochemical Perspectives Letters 23, 43–48. Scopus. https://doi.org/10.7185/geochemlet.2236.

Ahmad, Q., Wille, M., Labidi, J., König, S., Devey, C., Mezger, K., 2023. Heavy Mo isotope enrichment in the Pitcairn plume: Implications for the subduction cycle of anoxic sediments. Earth Planet. Sci. Lett. 624, 118466 https://doi.org/10.1016/j.epsl.2023.118466.

Aldrian, E., Dwi Susanto, R., 2003. Identification of three dominant rainfall regions within Indonesia and their relationship to sea surface temperature. Int. J. Climatol. 23 (12), 1435–1452. https://doi.org/10.1002/joc.950.

Archer, C., Vance, D., 2008. The isotopic signature of the global riverine molybdenum flux and anoxia in the ancient oceans. Nat. Geosci. 1 (9), 597–600. https://doi.org/10.1038/ngeo282.

Babechuk, M.G., Widdowson, M., Kamber, B.S., 2014. Quantifying chemical weathering intensity and trace element release from two contrasting basalt profiles, Deccan Traps, India. Chem. Geol. 363, 56–75. https://doi.org/10.1016/j.chemgeo.2013.10.027.

Barling, J., Anbar, A.D., 2004. Molybdenum isotope fractionation during adsorption by manganese oxides. Earth Planet. Sci. Lett. 217 (3–4), 315–329. https://doi.org/10.1016/S0012-821X(03)00608-3.

Barling, J., Arnold, G.L., Anbar, A.D., 2001. Natural mass-dependent variations in the isotopic composition of molybdenum. Earth Planet. Sci. Lett. 193 (3–4), 447–457. https://doi.org/10.1016/S0012-821X(01)00514-3.

Beinlich, A., Austrheim, H., Mavromatis, V., Grguric, B., Putnis, C.V., Putnis, A., 2018. Peridotite weathering is the missing ingredient of Earth's continental crust composition. Nat. Commun. 9 (1), 634. https://doi.org/10.1038/s41467-018-03039-9.

Bezard, R., Guo, H., 2023. Fluid-melt Mo isotope fractionation: Implications for the δ98/95Mo of the upper crust. Geochemical Perspectives Letters 26, 25–30. https://doi.org/10.7185/geochemlet.2320.

Chappaz, A., Lyons, T.W., Gordon, G.W., Anbar, A.D., 2012. Isotopic Fingerprints of Anthropogenic Molybdenum in Lake Sediments. Environ. Sci. Technol. 46 (20), 10934–10940. https://doi.org/10.1021/es3019379.

Chen, S., Hin, R.C., John, T., Brooker, R., Bryan, B., Niu, Y., Elliott, T., 2019. Molybdenum systematics of subducted crust record reactive fluid flow from underlying slab serpentine dehydration. Nat. Commun. 10 (1) https://doi.org/10.1038/s41467-019-12696-3. Article 1.

Collier, R.W., 1985. Molybdenum in the Northeast Pacific Ocean. Limnol. Oceanogr. 30 (6), 1351–1354. https://doi.org/10.4319/lo.1985.30.6.1351.

Colodner, D., Edmond, J., Boyle, E., 1995. Rhenium in the Black Sea: Comparison with molybdenum and uranium. Earth Planet. Sci. Lett. 131 (1), 1–15. https://doi.org/10.1016/0012-821X(95)00010-A.

Costa, K.M., Russell, J.M., Vogel, H., Bijaksana, S., 2015. Hydrological connectivity and mixing of Lake Towuti, Indonesia in response to paleoclimatic changes over the last 60,000 years. Palaeogeogr. Palaeoclimatol. Palaeoecol. 417, 467–475. https://doi.org/10.1016/j.palaeo.2014.10.009.

Dai, F.-Q., Chen, Y.-X., Chen, R.-X., Zhao, Z.-F., Li, J., Wang, Y., 2024. Subducted serpentinite contributes to the formation of arc lavas with heavy Mo isotopic compositions. Geochim. Cosmochim. Acta 369, 62–70. https://doi.org/10.1016/j.gca.2024.01.033.

Emerson, S.R., Huested, S.S., 1991. Ocean anoxia and the concentrations of molybdenum and vanadium in seawater. Mar. Chem. 34 (3–4), 177–196. https://doi.org/10.1016/0304-4203(91)90002-E.

Fan, J.-J., Li, J., Wang, Q., Zhang, L., Zhang, J., Zeng, X.-L., Ma, L., Wang, Z.-L., 2020. High-precision molybdenum isotope analysis of low-Mo igneous rock samples by MC–ICP–MS. Chem. Geol. 545, 119648 https://doi.org/10.1016/j.chemgeo.2020.119648.

Feng, L., Zhou, L., Hu, W., Zhang, W., Li, B., Liu, Y., Hu, Z., Yang, L., 2020. A simple single-stage extraction method for Mo separation from geological samples for isotopic analysis by MC-ICP-MS. J. Anal. At. Spectrom. 35 (1), 145–154. https://doi.org/10.1039/C9JA00267G.

Goldberg, S., Forster, H.S., Godfrey, C.L., 1996. Molybdenum Adsorption on Oxides, Clay Minerals, and Soils. Soil Sci. Soc. Am. J. 60 (2), 425–432. https://doi.org/10.2136/sssaj1996.03615995006000020013x.

Goldberg, T., Archer, C., Vance, D., Poulton, S.W., 2009. Mo isotope fractionation during adsorption to Fe (oxyhydr)oxides. Geochim. Cosmochim. Acta 73 (21), 6502–6516. https://doi.org/10.1016/j.gca.2009.08.004.

Goldberg, T., Gordon, G., Izon, G., Archer, C., Pearce, C.R., McManus, J., Anbar, A.D., Rehkämper, M., 2013. Resolution of inter-laboratory discrepancies in Mo isotope data: an intercalibration. J. Anal. At. Spectrom. 28 (5), 724–735. https://doi.org/10.1039/c3ja30375f.

Greaney, A.T., Rudnick, R.L., Romaniello, S.J., Johnson, A.C., Anbar, A.D., Cummings, M.L., 2021. Assessing molybdenum isotope fractionation during continental weathering as recorded by weathering profiles in saprolites and bauxites. Chem. Geol. 566, 120103 https://doi.org/10.1016/j.chemgeo.2021.120103.

Greber, N.D., Siebert, C., Nägler, T.F., Pettke, T., 2012. δ $^{98/95}$ Mo values and Molybdenum Concentration Data for NIST SRM 610, 612 and 3134: Towards a Common Protocol for Reporting Mo Data. Geostand. Geoanal. Res. 36 (3), 291–300. https://doi.org/10.1111/j.1751-908X.2012.00160.x.

Greber, N.D., Pettke, T., Nägler, T.F., 2014. Magmatic–hydrothermal molybdenum isotope fractionation and its relevance to the igneous crustal signature. Lithos 190–191, 104–110. https://doi.org/10.1016/j.lithos.2013.11.006.

Hall, R., Wilson, M.E.J., 2000. Neogene sutures in eastern Indonesia. J. Asian Earth Sci. 18 (6), 781–808. https://doi.org/10.1016/S1367-9120(00)00040-7.

Hamilton, W., 1973. Tectonics of the Indonesian Region. Bulletin of the Geological Society of Malaysia 6, 3–10. https://doi.org/10.7186/bgsm06197301.

Harkness, J.S., Sulkin, B., Vengosh, A., 2016. Evidence for Coal Ash Ponds Leaking in the Southeastern United States. Environ. Sci. Technol. 50 (12), 6583–6592. https://doi.org/10.1021/acs.est.6b01727.

Hendon, H.H., 2003. Indonesian Rainfall Variability: Impacts of ENSO and Local Air–Sea Interaction. J. Clim. 16 (11), 1775–1790. https://doi.org/10.1175/1520-0442(2003)016<1775:IRVIOE>2.0.CO;2.

Hongve, D., 1997. Cycling of iron, manganese, and phosphate in a meromictic lake. Limnol. Oceanogr. 42 (4), 635–647. https://doi.org/10.4319/lo.1997.42.4.0635.
Hopp, T., Fischer-Gödde, M., Kleine, T., 2016. Ruthenium stable isotope measurements by double spike MC-ICPMS. J. Anal. At. Spectrom. 31 (7), 1515–1526. https://doi.org/10.1039/C6JA00041J.
Horan, K., Hilton, R.G., McCoy-West, A.J., Selby, D., Tipper, E.T., Hawley, S., Burton, K. W., 2020. Unravelling the controls on the molybdenum isotope ratios of river waters. Geochemical Perspectives Letters 1–6. https://doi.org/10.7185/geochemlet.2005.
Kadarusman, A., Miyashita, S., Maruyama, S., Parkinson, C.D., Ishikawa, A., 2004. Petrology, geochemistry and paleogeographic reconstruction of the East Sulawesi Ophiolite, Indonesia. Tectonophysics 392 (1–4), 55–83. https://doi.org/10.1016/j.tecto.2004.04.008.
Katili, J.A., 1978. Past and present geotectonic position of Sulawesi, Indonesia. Teetonophysics 45, 289–322. https://doi.org/10.1016/0040-1951(78)90166-X.
Kaufmann, A.K.C., Pettke, T., Wille, M., 2021. Molybdenum isotope fractionation at upper-crustal magmatic-hydrothermal conditions. Chem. Geol. 578, 120319 https://doi.org/10.1016/j.chemgeo.2021.120319.
Kendall, B., Dahl, T.W., Anbar, A.D., 2017. The Stable Isotope Geochemistry of Molybdenum. Rev. Mineral. Geochem. 22, 683–732. https://doi.org/10.2138/rmg.2017.82.16.
King, E.K., Thompson, A., Chadwick, O.A., Pett-Ridge, J.C., 2016. Molybdenum sources and isotopic composition during early stages of pedogenesis along a basaltic climate transect. Chem. Geol. 445, 54–67. https://doi.org/10.1016/j.chemgeo.2016.01.024.
Koschinsky, A., Hein, J.R., 2003. Uptake of elements from seawater by ferromanganese crusts: Solid-phase associations and seawater speciation. Mar. Geol. 198 (3–4), 331–351. https://doi.org/10.1016/S0025-3227(03)00122-1.
Kurniadi, A., Weller, E., Min, S.-K., Seong, M.-G., 2021. Independent ENSO and IOD impacts on rainfall extremes over Indonesia. Int. J. Climatol. 41 (6), 3640–3656. https://doi.org/10.1002/joc.7040.
Larsen, K.K., Wielandt, D., Schiller, M., Bizzarro, M., 2016. Chromatographic speciation of Cr(III)-species, inter-species equilibrium isotope fractionation and improved chemical purification strategies for high-precision isotope analysis. J. Chromatogr. A 1443, 162–174. https://doi.org/10.1016/j.chroma.2016.03.040.
Liang, Y.-H., Halliday, A.N., Siebert, C., Fitton, J.G., Burton, K.W., Wang, K.-L., Harvey, J., 2017. Molybdenum isotope fractionation in the mantle. Geochim. Cosmochim. Acta 199, 91–111. https://doi.org/10.1016/j.gca.2016.11.023.
Liu, J.-H., Zhou, L., Algeo, T.J., Wang, X.-C., Wang, Q., Wang, Y., Chen, M.-L., 2020. Molybdenum isotopic behavior during intense weathering of basalt on Hainan Island, South China. Geochim. Cosmochim. Acta 287, 180–204. https://doi.org/10.1016/j.gca.2020.04.018.
Miller, C.A., Peucker-Ehrenbrink, B., Walker, B.D., Marcantonio, F., 2011. Re-assessing the surface cycling of molybdenum and rhenium. Geochim. Cosmochim. Acta 75 (22), 7146–7179. https://doi.org/10.1016/j.gca.2011.09.005.
Monnier, C., Girardeau, J., Maury, R.C., Cotten, J., 1995. Back-arc basin origin for the East Sulawesi ophiolite (eastern Indonesia). Geology 23 (9), 851–854. https://doi.org/10.1130/0091-7613(1995)023<0851:BABOFT>2.3.CO;2.
Morlock, M.A., Vogel, H., Nigg, V., Ordoñez, L., Hasberg, A.K.M., Melles, M., Russell, J. M., Bijaksana, S., the TDP Science Team, 2019. Climatic and tectonic controls on source-to-sink processes in the tropical, ultramafic catchment of Lake Towuti, Indonesia. J. Paleolimnol. 61 (3), 279–295. https://doi.org/10.1007/s10933-018-0059-3.
Mubroto, B., Briden, J.C., McClelland, E., Hall, R., 1994. Palaeomagnetism of the Balantak ophiolite, Sulawesi. Earth Planet. Sci. Lett. 125 (1–4), 193–209. https://doi.org/10.1016/0012-821X(94)90215-1.
Nägler, T., Pierret, M.-C., Voegelin, A., Pettke, T., Aschwanden, L., Villa, I., 2020. Small Catchment Scale Molybdenum Isotope Balance and its Implications for Global Molybdenum Isotope Cycling. In: Biogeochemical Cycles. American Geophysical Union (AGU), pp. 163–189. https://doi.org/10.1002/9781119413332.ch8.
Nakagawa, Y., Takano, S., Firdaus, M.L., Norisuye, K., Hirata, T., Vance, D., Sohrin, Y., 2012. The molybdenum isotopic composition of the modern ocean. Geochem. J. 46 (2), 131–141. https://doi.org/10.2343/geochemj.1.0158.
Neely, R.A., Gislason, S.R., Ólafsson, M., McCoy-West, A.J., Pearce, C.R., Burton, K.W., 2018. Molybdenum isotope behaviour in groundwaters and terrestrial hydrothermal systems, Iceland. Earth Planet. Sci. Lett. 486, 108–118. https://doi.org/10.1016/j.epsl.2017.11.053.
Nesbitt, H.W., Young, G.M., 1982. Early Proterozoic climates and plate motions inferred from major element chemistry of lutites. Nature 299 (5885), 715–717. https://doi.org/10.1038/299715a0.
Neubert, N., Heri, A.R., Voegelin, A.R., Nägler, T.F., Schlunegger, F., Villa, I.M., 2011. The molybdenum isotopic composition in river water: Constraints from small catchments. Earth Planet. Sci. Lett. 304 (1–2), 180–190. https://doi.org/10.1016/j.epsl.2011.02.001.
O'Sullivan, E.M., Nägler, T.F., Babechuk, M.G., 2021. Unusually heavy stable Mo isotope signatures of the Ottawa River: Causes and implications for global riverine Mo fluxes. Chem. Geol. 568, 120039 https://doi.org/10.1016/j.chemgeo.2020.120039.
O'Sullivan, E.M., Nägler, T.F., Turner, E.C., Kamber, B.S., Babechuk, M.G., O'Hare, S.P., 2022. Mo isotope composition of the 0.85 Ga Ocean from coupled carbonate and shale archives: some implications for pre-Cryogenian oxygenation. Precambrian Res. 378, 106760 https://doi.org/10.1016/j.precamres.2022.106760.
Parkinson, C., 1998. Emplacement of the East Sulawesi Ophiolite: evidence from subophiolite metamorphic rocks. J. Asian Earth Sci. 16 (1), 13–28. https://doi.org/10.1016/S0743-9547(97)00039-1.
Pearce, C.R., Burton, K.W., Von Strandmann, P.A.E.P., James, R.H., Gíslason, S.R., 2010. Molybdenum isotope behaviour accompanying weathering and riverine transport in a basaltic terrain. Earth Planet. Sci. Lett. 295 (1–2), 104–114. https://doi.org/10.1016/j.epsl.2010.03.032.
Ptáček, M.P., Dauphas, N., Greber, N.D., 2020. Chemical evolution of the continental crust from a data-driven inversion of terrigenous sediment compositions. Earth Planet. Sci. Lett. 539, 116090 https://doi.org/10.1016/j.epsl.2020.116090.
Revels, B.N., Rickli, J., Moura, C.A.V., Vance, D., 2021. The riverine flux of molybdenum and its isotopes to the ocean: Weathering processes and dissolved-particulate partitioning in the Amazon basin. Earth Planet. Sci. Lett. 559, 116773 https://doi.org/10.1016/j.epsl.2021.116773.
Rojas-Kolomiets, E., Jensen, O., Bizimis, M., Yogodzinski, G., Ackerman, L., 2023. Serpentinite fluids and slab-melting in the Aleutian arc: evidence from molybdenum isotopes and boron systematics. Earth Planet. Sci. Lett. 603, 117970 https://doi.org/10.1016/j.epsl.2022.117970.
Siebert, C., Nägler, T.F., Kramers, J.D., 2001. Determination of molybdenum isotope fractionation by double-spike multicollector inductively coupled plasma mass spectrometry. Geochem. Geophys. Geosyst. 2 (7) https://doi.org/10.1029/2000GC000124, 2000GC000124.
Siebert, C., Nägler, T.F., Von Blanckenburg, F., Kramers, J.D., 2003. Molybdenum isotope records as a potential new proxy for paleoceanography. Earth Planet. Sci. Lett. 211 (1–2), 159–171. https://doi.org/10.1016/S0012-821X(03)00189-4.
Siebert, C., Pett-Ridge, J.C., Opfergelt, S., Guicharnaud, R.A., Halliday, A.N., Burton, K. W., 2015. Molybdenum isotope fractionation in soils: Influence of redox conditions, organic matter, and atmospheric inputs. Geochim. Cosmochim. Acta 162, 1–24. https://doi.org/10.1016/j.gca.2015.04.007.
Villeneuve, M., Gunawan, W., Cornee, J.-J., Vidal, O., 2002. Geology of the Central Sulawesi belt (eastern Indonesia): Constraints for geodynamic models. Int. J. Earth Sci. 91 (3), 524–537. https://doi.org/10.1007/s005310100228.
Voegelin, A.R., Nägler, T.F., Pettke, T., Neubert, N., Steinmann, M., Pourret, O., Villa, I. M., 2012. The impact of igneous bedrock weathering on the Mo isotopic composition of stream waters: Natural samples and laboratory experiments. Geochim. Cosmochim. Acta 86, 150–165. https://doi.org/10.1016/j.gca.2012.02.029.
Voegelin, A.R., Pettke, T., Greber, N.D., von Niederhäusern, B., Nägler, T.F., 2014. Magma differentiation fractionates Mo isotope ratios: evidence from the Kos Plateau Tuff (Aegean Arc). Lithos 190–191, 440–448. https://doi.org/10.1016/j.lithos.2013.12.016.
Wang, Z., Becker, H., 2018. Molybdenum partitioning behavior and content in the depleted mantle: Insights from Balmuccia and Baldissero mantle tectonites (Ivrea Zone, Italian Alps). Chem. Geol. 499, 138–150. https://doi.org/10.1016/j.chemgeo.2018.09.023.
Wang, Z., Ma, J., Li, J., Wei, G., Chen, X., Deng, W., Xie, L., Lu, W., Zou, L., 2015. Chemical weathering controls on variations in the molybdenum isotopic composition of river water: evidence from large rivers in China. Chem. Geol. 410, 201–212. https://doi.org/10.1016/j.chemgeo.2015.06.022.
Wang, Z., Ma, J., Li, J., Wei, G., Zeng, T., Li, L., Zhang, L., Deng, W., Xie, L., Liu, Z., 2018. Fe (hydro) oxide controls Mo isotope fractionation during the weathering of granite. Geochim. Cosmochim. Acta 226, 1–17. https://doi.org/10.1016/j.gca.2018.01.032.
Wang, Z., Ma, J., Li, J., Zeng, T., Zhang, Z., He, X., Zhang, L., Wei, G., 2020. Effect of Fe–Ti oxides on Mo isotopic variations in lateritic weathering profiles of basalt. Geochim. Cosmochim. Acta 286, 380–403. https://doi.org/10.1016/j.gca.2020.07.030.
Widdowson, M., 2007. Laterite and ferricretes. In: Geochemical Sediments and Landscapes, 1st ed. Blackwell Publishing Ltd., pp. 46–94
Willbold, M., Elliott, T., 2017. Molybdenum isotope variations in magmatic rocks. Chem. Geol. 449, 253–268. https://doi.org/10.1016/j.chemgeo.2016.12.011.
Willbold, M., Hibbert, K., Lai, Y.-J., Freymuth, H., Hin, R.C., Coath, C., Vils, F., Elliott, T., 2016. High-Precision Mass-Dependent Molybdenum Isotope Variations in Magmatic Rocks Determined by Double-Spike MC-ICP-MS. Geostand. Geoanal. Res. 389–403 https://doi.org/10.1111/ggr.12109.
Wille, M., Nebel, O., Van Kranendonk, M.J., Schoenberg, R., Kleinhanns, I.C., Ellwood, M.J., 2013. Mo–Cr isotope evidence for a reducing Archean atmosphere in 3.46–2.76Ga black shales from the Pilbara, Western Australia. Chem. Geol. 340, 68–76. https://doi.org/10.1016/j.chemgeo.2012.12.018.
Xu, X.-R., Li, H.-B., Li, X.-Y., Gu, J.-D., 2004. Reduction of hexavalent chromium by ascorbic acid in aqueous solutions. Chemosphere 57 (7), 609–613. https://doi.org/10.1016/j.chemosphere.2004.07.031.
Yang, J., Barling, J., Siebert, C., Fietzke, J., Stephens, E., Halliday, A.N., 2017. The molybdenum isotopic compositions of I-, S- and A-type granitic suites. Geochim. Cosmochim. Acta 205, 168–186. https://doi.org/10.1016/j.gca.2017.01.027.
Zhao, P., Li, J., Zhang, L., Wang, Z., Kong, D., Ma, J., Wei, G., Xu, J., 2016. Molybdenum Mass Fractions and Isotopic Compositions of International Geological Reference Materials. Geostand. Geoanal. Res. 40 (2), 217–226. https://doi.org/10.1111/j.1751-908X.2015.00373.x.